Accelerated/reduced growth of tungsten fuzz by deposition of metals

Shin Kajita

Institute of Materials and Systems for Sustainability, Nagoya University, Nagoya 464-8603, Japan

Thomas Morgan

DIFFER - Dutch Institute for Fundamental Energy Research, De Zaale 20, 5612 AJ Eindhoven, the Netherlands

Hirohiko Tanaka

Graduate School of Engineering, Nagoya University, Nagoya 464-8603, Japan

Yuki Hayashi

National Institute for Fusion Science, 322-6 Oroshi-cho, Toki, 509-5292 Japan

Naoaki Yoshida

Research Institute for Applied Mechanics, Kyushu University, Kasuga, Fukuoka 816-8580, Japan

Daisuke Nagata

National Institute for Fusion Science, 322-6 Oroshi-cho, Toki, 509-5292 Japan

Jordy Vernimmen

DIFFER - Dutch Institute for Fundamental Energy Research, De Zaale 20, 5612 AJ Eindhoven, the Netherlands

Shuangyuan Feng, Rongshi Zhang, Noriyasu Ohno

Graduate School of Engineering, Nagoya University, Nagoya 464-8603, Japan

Abstract

From the helium (He) plasma irradiations to tungsten performed in the Magnum-PSI device, the effects of deposition of metals on the helium-plasma induced fiberform nanostructures (fuzz) are discussed. It was found that fuzz was not formed at the center of the plasma cylinder if there were significant metallic impurities from the source. Deposition of metallic impurities (mainly molybdenum and copper) counteracted the growth of fuzz. In addition to the effects of metals from the source, we installed a sputtering source near the sample to replicate the deposition environment in fusion devices. The thickness of fuzzy layer was ~7 μm, which was about five times greater than that without deposition, at the He flux of 1.3×10^{26} m^{-2}, suggesting that the growth rate of fuzz layer was significantly accelerated due to the deposition of tungsten.

1. Introduction

Plasma-facing components in fusion devices are subjected to deuterium (D), helium (He), and some impurities such as argon, neon, and nitrogen, which are used as radiators to cool down the edge plasma. Among them, the He effects lead to various morphology changes on tungsten (W) including helium bubbles [1], blisters [2], and fiberform nanostructures (FNs), so called *fuzz* [3], which is arguably the most significant morphology change to occur in fusion-relevant conditions. Concerning the fuzz growth, extensive experimental investigations have been conducted to reveal the phenomenon from various aspects: growth condition [4], growth rate [5, 6], annealing phenomena [7, 8, 9], and sputtering effect [10, 11, 12]. A recent model including the growth and annealing effects has revealed that thickness of the fuzzy layer, h_{FN}, depends on the base temperature, the energy density from edge localized modes (ELMs), and the frequency of ELMs [13].

In addition to the above known effects, recent studies have revealed that co-deposition could be another influential effect for the growth of fuzz [14]. Various effects of deposition of metals (W and other materials) on He induced morphology changes have been discussed to date. For example, it was discussed based on experiments with small amounts of impurities (argon, neon, and nitrogen) that the isolated nanostructures called nano-tendril bundles formed in He plasmas could be related to

Email address: kajita.shin@nagoya-u.jp (Shin Kajita)

the deposition of sputtered W [15]. Also, it has been revealed that mm-thick large-scale fiberform nanostructures (LFNs) can be formed at an accelerated growth rate with an additional deposition [16, 17]. In the Magnum-PSI device, plasma irradiations to a W monoblock mockup have revealed that metallic impurities from the source led to some unexpected phenomena such as an enhanced diffusion of molybdenum (Mo) along the grain boundaries and sponge-like tin structures [18]. In short, the effects of deposition of metals on He plasma induced morphology changes have not been fully understood, and they will be important to assess the impact of He effects in fusion devices. Concerning the accelerated growth of fuzz by an auxiliary deposition, the effects have been identified in two devices (NAGDIS-II and a magnetron sputtering device). It is important to investigate the effects in other devices, particularly under higher plasma density conditions, because the transport of metals could be altered with increasing the density.

In this study, we investigate He plasma irradiation of W, focusing on metallic impurity effects in Magnum-PSI in two different ways. First, we conduct pure He plasma irradiation and discuss the relations between non-uniformity in the fuzz growth and irradiation parameters including impurities from the plasma source. A sputtering source is then installed near the sample to investigate the auxiliary deposition effects.

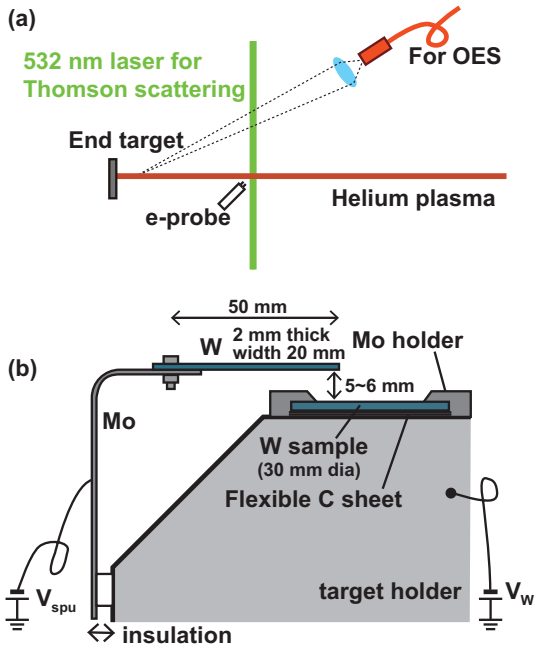

Figure 1: (a) A schematic of the experimental setup in Magnum-PSI and (b) a schematic around the end target and sputtering plate for deposition experiments.

2. Experimental setup

Figure 1(a) shows a schematic of the experimental setup in Magnum-PSI [19]. In Magnum-PSI, a beam shaped plasma can be produced in a steady state, and the density and temperature are able to be measured by a laser Thomson scattering (TS) system [20]. The axial position of the TS measurement was at ~30 cm from the target. The typical density and temperature ranges in the Magnum-PSI were respectively, 1–10×10^{20} m^{-3} and 0.3–5 eV [21]. At the same axial position, we installed a reciprocating probe. Although it was available only for some irradiation cases, we can deduce the profiles of the space potential (plasma potential), which were not obtained from the TS measurements, by using the probe. Several spectrometers (Avantes AvaSpec-2048) are available for optical emission spectroscopy (OES) in Magnum-PSI, and one of them (which saw the target view) was used to observe the emission from the plasma.

A 1-mm-thick W sample (poly crystal, > 99.97% W) with 30 mm diameter (Plansee) was equipped on the end target without any pretreatment. The sample was fixed on the sample holder with a flexible carbon sheet (GRAFOIL) behind. The surface temperature, T_s, was measured from the radiation in the near infrared range. A multi-wavelength pyrometer (type FMPI, Far Associates) [22], which does not require prior knowledge of emissivity, was used. Used wavelength range was from 1.1 to 1.7 μm. The sample temperature during the irradiation was determined from the balance between the heat load and the thermal conductance to the target holder. Source setting was varied to control the surface temperature; however, since the sample was tightly clamped on the sample holder, it was sometimes too low to reach the minimum fuzz growth temperature of 900–1000 K [4, 23] when the plasma density was low. Thus, in some cases, we made a hole on the GRAFOIL to increase the thermal resistance between the sample and target holder. The sample was biased together with the holder to V_W by an electric power supply.

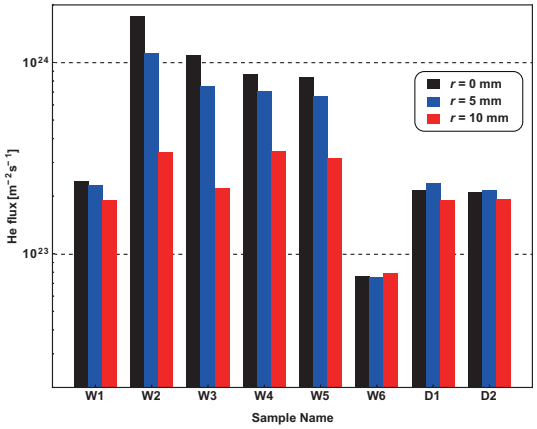

Figure 2: Helium fluxes at different positions (black: r = 0 mm, blue: r = 5 mm, and red: r = 10 mm) for the samples W1-W6 and D1-D2. The voltage of the sample (V_W) was different between samples W1-W6 (W1: -13V, W2: -22 V, W3: -34 V, W4: -45 V, W5: -55 V, and W6: -62 V) and T_s ranged 1100-1370 K. No sputtering source was installed for W1-W6 samples, while sputtering plate was installed and biased to -250–300 V for D1 and D2.

In addition to pure He plasma irradiation, we investigated the effect of deposition with an additional impurity source. Figure 1(b) shows a schematic of the setup around the target for the deposition experiments. A 2-mm-thick W target, which had a width of 20 mm, was installed near the sample. The distance from the sample to the sputtering target was 5-6 mm. The sample and sputtering target were electrically isolated and could be

biased separately. Table 1 summarizes the irradiation conditions. The samples named W1-W6 are exposed to He plasmas without W deposition, and D1 and D2 are the samples exposed to He plasmas with an additional W deposition. For samples W1-W6, the biasing voltage was altered and T_s ranged from 1100 to 1370 K. Because the temperature of the sputtering target increased significantly and it emitted significant radiation, we could not measure T_s due to the reflection of the radiation from the sputtering target. It was likely that T_s of D1 and D2 was close to W1 (1320 K), because the He flux was similar, as shown next.

Figure 2 shows He flux, Γ_{He} for the eight samples in Table 1 at three different positions from the center, r, of 0, 5, and 10 mm.

The He flux was determined using the electron density, n_e, and the temperature, T_e, measured by TS from the following relation:

$$\Gamma_{\mathrm{He}} = 0.5 n_e \sqrt{\frac{2eT_e}{m_{\mathrm{He}}}}. \quad (1)$$

Here, e is the elementary charge in C, m_{He} is the mass of a He atom, and we assumed that the ion temperature is equal to T_e, and that the density at the sheath edge is half of the bulk electron density (n_e) [24]. The He flux was $\sim 10^{24}$ $\mathrm{m^{-2}s^{-1}}$ on W2-W5 at the center of the plasma column, while it was less than 3×10^{23} $\mathrm{m^{-2}s^{-1}}$ on W1, W6, D1, and D2. This was mainly because a hole was made on the GRAFOIL for W1, W6, D1, and D2; low density plasmas were enough to increase T_s to higher than 1000 K.

Concerning D1 and D2, the sputtering target was installed and biased to -250 and -300 V, respectively. Because the incident ion energy was high and no active cooling was available, the temperature of the sputtering target increased quickly. Thus, we could not continue the irradiation for a long time. We repeated transient irradiations for 25 or 20 s and accumulated the irradiation time to 600 s, which was one third of the duration for W1-W6.

3. Non-uniform fuzz growth

3.1. Morphology changes

Figure 3(a-f) shows pictures of W1-W6 samples, respectively, after the exposures. Visually, no significant change was identified on W1. Blackening occurred at the peripheral region of W2, W3, and W4, and the blackened areas on W2 and W4 had non-uniformity. Although W5 surface did not become black, small black spots were found on the peripheral region, while the center of the plasma column became white. Blackening occurred on the whole surface of W6.

Figure 4(a-c), (d-f), (g-i), (j-l), (m-o), and (p-r) shows SEM micrographs of W1, W2, W3, W4, W5, and W6, respectively, at three different locations, i.e. at the center (a,d,g,j,m,p), $r = 2-5$ mm (b,e,h,k,n,q), and $5-10$ mm (c,f,i,l,o,r), where r is the distance from the irradiation center, which was defined by visual observation. As was seen in the pictures (Fig. 3(a)), almost no changes were identified on W1 even with SEM analysis. On

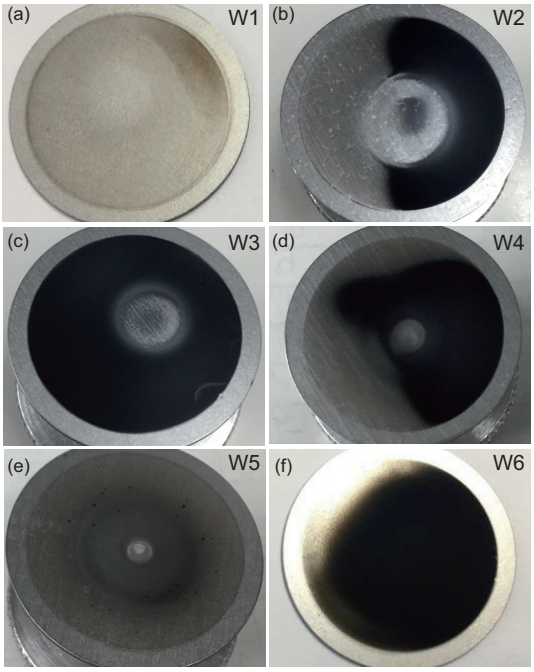

Figure 3: (a-f) Pictures of W1-W6 samples, respectively. The potential of the sample (V_W) was (a) -13V, (b) -22 V, (c) -34 V, (d) -45 V, (e) -55 V, and (f) -62 V.

W2-W4, fuzz was grown at $r = 5-10$ mm, while protrusions were formed around the center. The protrusions on the central region of W2 and W4 (Fig. 4(d,j)) were similar to initial stages of fuzz growth; the rough surface formed around the center of W3 (Fig. 4(g)) seemed to be caused by deposition. On W5, even though the potential of the sample, V_W, was deeper than that of W1-4, the fuzz growth did not occur, while fuzz growth occurred in the peripheral region locally. Fig. 4(o) shows a part of the locally formed fuzz, and whiskers are seen on the left half side. The details of the isolated structures are shown next. Fuzz was fully grown in the whole surface area on W6 (Fig. 4(p-r)).

Figure 5(a-c) shows SEM micrographs of the peripheral region of W5 at different magnifications. In Fig. 5(a), many white spots with various sizes can be identified. At a low magnification, as shown in Fig. 5(b), a white spot has a patchy texture. And at a high magnification, it is seen that fuzz is grown in the white areas, as in Fig. 5(c).

3.2. Discussion

It is understandable that no changes occurred on W1, because the incident ion energy, E_i, should be lower than the threshold energy for fuzz growth of ~20 eV. The threshold energy could be lower than 20 eV especially when the He fluence is high [3, 18], but E_i on W1 was likely too low to lead to nanostructuring. And, also, the result of W6 (fuzz growth on the whole sample area) was reasonable, because both of E_i and T_s satisfied the necessary condition for fuzz growth. However, the profiles of the morphology change on W2-W5 sample were not straightforward to understand. Three questions arose about the morphology changes of W2-W5: (i) Why did fuzz growth not occur in the central region on W2-W5? (ii) Why was there

Table 1: Experimental conditions for the preparation of the samples used in this study. The shown parameters are as follows: the sample potential (V_W), the surface temperature (T_s), the potential of the sputtering plate (V_{spu}), duration, and He fluence. The maximum values at the irradiation center are shown for T_s and He fluence.

Name	V_W [V]	T_s [K]	V_{spu} [V]	Duration [s]	He fluence [m^{-2}]
W1	-13	1320	–	1800	4.3×10^{26}
W2	-22	1140±15	–	1800	3.1×10^{27}
W3	-34	1230±29	–	1800	2.0×10^{27}
W4	-45	1120±12	–	1800	1.6×10^{27}
W5	-55	1100±10	–	1800	1.5×10^{27}
W6	-62	1360±20	–	1800	1.4×10^{26}
D1	-83	–	-250	600 (25 s×24)	1.3×10^{26}
D2	-81	–	-300	600 (20 s×30)	1.3×10^{26}

non-uniformity in the fuzz growth in the peripheral region of W2 and W4? (iii) Why did non-uniform isolated fuzz growth occur on W5?

For the fuzz growth by He plasma irradiation, E_i and T_s are important parameters. Concerning E_i, in addition to the potential of the target, the space potential of the plasma is also important. Figure 6 shows two potential profiles for the irradiation conditions of W1 and W6 measured using the reciprocating probe. When balancing the ion current and election current, the floating potential, V_f, can be expressed as [25]

$$V_f = V_s + \frac{T_e}{2}\ln\left[\frac{2\pi m_e}{m_{\rm He}}\left(1+\frac{T_i}{T_e}\right)\right] - \frac{T_e}{2}, \quad (2)$$

where m_e is the mass of an electron, V_s is the space potential, and T_i is the ion temperature. Here, the potential drop in presheath by $-T_e/2$ was also take into consideration. Thus, the space potential can be deduced from the floating potential measured by the probe and T_e from TS under the assumption of $T_i = T_e$ as

$$V_s = V_f + 3.7T_e. \quad (3)$$

The potential has a well-shaped profile in both of the cases, though the potential depth alters depending on the discharge condition. One of the reasons to form fuzz only at the periphery is in this potential profile, which leads to a lower E_i at the center than that at the periphery.

Non-uniform blackening occurred at the periphery of W2 and W4 was probably because the temperature profile had a non-uniformity. Even if the heat flux from the plasma is uniform, a temperature non-uniformity can occur when thermal contact resistance between the sample and the sample holder has a non-uniform distribution. Although we cramped the sample to the holder using six screws with a same torque, non-uniformity in the thermal contact resistivity can occur because of surface roughness, cleanliness, deformation, etc. Note that no hole was made on GRAFOIL for W2 and W4 irradiation. At the contact surface, a temperature gap can be formed [26], and the temperature gap is a product of the heat flux and the thermal contact resistance. The heat load from the plasma can be expressed as [27]

$$Q = \Gamma_i\left[(2eT_i - eE_i)(1-R_E) + E_{\rm rec}\right], \quad (4)$$

where Γ_i is the ion flux, e is the elementary charge, R_E is ion reflection coefficient, and $E_{\rm rec}$ is the recombination energy (24.6 eV). For W2 or W4, Γ_i at 10 mm is $\approx 3\times10^{23}$ $m^{-2}s^{-1}$, and Q is assessed to be 1.9 MW/m^2. The thermal contact resistance can be varied significantly from $0.05 - 5\times10^{-4}$ m^2K/W depending on material, surface roughness, ambient gas (pressure) [26]. Using one of the available data in Ref. [26] of a milled copper surface with the roughness of 0.25 μm and vacuum gap (the thermal contact resistance of 0.88×10^{-4} m^2K/W) and the heat load of 2.3 MW/m^2, the temperature gap at the contact surface is assessed to be ≈160 K at E_i of 30 eV. Considering that the thermal conductivity of W is much lower than that of Cu, and the thermal contact resistance altered significantly with changing the pressure, a slight non-uniform contact at the rear surface of the sample can cause non-uniform thermal contact resistivity, and, consequently, a temperature difference by ∼ 100 K can occur under the present high heat flux conditions. It was likely that the blackened areas had a temperature higher than the threshold temperature for the fuzz growth of ≈1000 K, while the non-blackened area had a lower temperature than the threshold temperature.

In addition to E_i and T_s, here we investigate the effect of impurities. It is noted that crystal orientation and He fluence dependences are not important in this study. The crystal orientation dependence can appear in the initial growth phase [28], but it disappears when the fluence is sufficient ($> 10^{25}$ m^{-2}) at $E_i > 30$ eV. Also, the fluence is sufficiently high enough for the growth of fuzz in this study. First, spectroscopy will provide us information about the concentration of impurities. Figure 7(a) shows a typical measured spectrum in the wavelength range of 300-450 nm when W3 was exposed. In addition to He I lines at 388.9 and 447.1 nm, strong Cu I lines at 324.8 and 327. 4 nm and Ca II lines around 390-400 nm are identified. Although the intensity is weak, a Mo I line at 379.8 nm is recognized. Concerning Ca, it has been known that it was released from the source [29]. Figure 7(b) shows the line intensity ratios of Cu I at 324.8 nm and Mo I at 379.8 nm to He I at 447.1 nm for W1-W6 samples. It is seen that strong Cu I lines were observed while W2-W5 were exposed. This was mainly because high density plasma conditions were chosen, as shown in Fig. 2, and as a consequence, impurities were released from the source. It is noted that Mo I intensity is considerable when irradiating W5

sample.

We conducted energy-dispersive X-ray spectroscopy (EDS) analysis of several samples, and the results are summarized in Table 2. Here, in addition to the spectroscopically identified species (Mo, Cu, and Ca), we added iron to consider the influence of vacuum vessel. On W3, where fuzz was grown only at the edge, the center had a rather high (25.4%) Mo fraction, while the fraction was smaller where fuzz was grown. On the other hand, on W6, where fuzz was grown on the whole area, impurity level was less than 5%. The fraction of impurities (mainly Mo and copper (Cu)) was high at $r = 0$ mm on W5, as was suggested from spectroscopy shown in Fig. 7(b). The impurity fraction decreased at $r = 5$ mm. Concerning W5 sample, we performed EDS mapping around fuzz region at $r \sim 10$ mm, as shown in Figure 8 with two regions at different magnifications. Around the fuzz region in Fig. 8(a), the W signal level is lower than the region around (Fig. 8(b)), while the Mo signal does not have clear non-uniformity (Fig. 8(c)). In the region shown in Fig. 8(d), it seemed that the W signal decreased (Fig. 8(e)) in the white fuzzy region, and the Mo signal also has non-uniformity (Fig. 8(f)). To qualitatively discuss the impurity fractions, we analyzed the regions A, B, C, and D shown in Fig. 8(a,d). The results are summarized in Table 2. It is shown that the fuzz region has higher impurity concentration, but the impurity fraction is less than 10% from the top view observation. Since the influence of bulk could be included, we scraped the fuzzy material by a carbon tape and performed EDS analysis. The impurity fraction was much higher than the other region (24.9±11.9%), as shown in Table 2. It is likely that the value identified on the carbon tape is more plausible than that from top view analysis, because the bulk effect was eliminated by scraping off the structure.

When the biasing was not enough, E_i was not enough to form fuzz. This could be the cases of W1. Although the potential difference between $r = 0$ and 10 mm was not great, typically <5 V from Fig. 6, the difference could be crucial for W2 to cause the difference in the morphology changes at $r = 0$ and 10 mm, because the incident energy was likely to be close to the threshold energy of 20-30 eV. However, because fuzz did not form at the center even when deepening the potential from W2 to W5, it was likely that deposition of impurity counteracted the growth of fuzz around the center on W3-W5. There were two possible reasons why the impurity has prevented from growing fuzz. Since the ionized impurities have much greater sputtering rates than that of He, the sputtering process might have counteracted to fuzz growth. Another reason is that the temperature at the center is too high for the deposited metals to form fuzz, because impurities have much lower temperature ranges to form fuzz [30]. We measured the height difference around the border of the fuzz region on W4 using the CLSM, and it was found that the central region without fuzz was eroded by 2-3 μm compared to the region with fuzz. The result suggested that sputtering by impurity ions led to the erosion, which counteracted the fuzz growth around the center. From the impurity profiles measured by EDS, the impurities were likely concentrated around the center, though the mechanism was not clearly understood.

On W5, because T_s was 1100 K at the center, which was lower than other samples. Thus, the temperature at the periphery was likely lower than the threshold temperature, i.e. <1000 K, and fuzz was not formed at the peripheral region. Concerning the local isolated fuzzy islands, similar isolated fuzz balls have been identified previously after a long time irradiation [18, 31]. In this work, the fraction of Mo was found to be higher on the location where fuzzy islands were formed from the EDS analysis. By the increase of the impurity fraction, the temperature window for fuzz growth can be changed in terms of the variation in the melting point, T_m. It is known that T_m decreases with increasing the mixing rate. Concerning W-Mo alloy, the melting point decreases by ~200 K at the Mo fraction of 25% [32]. The temperature window can be more or less explained in T_s/T_m, and the T_s/T_m window was in the range of 0.25-0.6 for all the metals where fuzz was grown [30]. The minimum T_s/T_m value for fuzz growth was almost the same between W (0.27) and Mo (0.28). A decrease of T_m in 200 K will increase T_s/T_m by 0.015 if T_s is around 1000 K. If impurity mixing rate was locally high and T_s was slightly lower than 1000 K, there was a possibility that the condition of $T_s/T_m > 0.27$ was locally satisfied.

4. Deposition experiments

4.1. Accelerated growth

Figure 9(a,b) shows pictures of D1 and D2 samples, respectively. The surface became black even at the irradiation center, while the blackened area was slightly smaller than W3 and W6. Figure 9(c,d) shows SEM micrographs of D1 and D2, respectively, around the center of the blackened area. It is seen that fuzz is grown and the feature of fiberform nanostructures (FNs) is almost the same as that of W6 shown in Fig. 4(p-r). It is noted that the line intensity ratio of 324.8 nm to 447.1 nm was less than unity under the both conditions (0.9 for D1 and 0.7 for D2). From EDS analysis on both of the samples (Table 2), it was found that the fraction of W was higher than 90% at $r = 0$ and 5 mm.

We measured the thickness of FN layer, h_{FN}, using a confocal laser scanning microscope (CLSM) (Keyence, VK-9700, 408 nm) by measuring the height profile after making a scratch on the sample, as was done in Ref. [6]. Figure 10(a,b) shows the depth profiles around scratches on W6 and D2 samples, respectively. The depth of the scratch on D2 is much deeper than that of W6. It was measured that h_{FN} on W6, D1, and D2 was 1.4±0.3, 7.0±0.2, and 6.8±0.5, respectively. To check this scratch method, the sample D1 was cut by a focused ion beam (FIB), and an SEM micrograph of the cross section was taken, as shown in Fig. 10(c). It is seen that the scratch, which is in the right side in Fig. 10(c), has wiped the fuzzy layer completely, and h_{FN} was measured to be 7.0 μm, which was consistent with the CLSM.

In Fig. 11, a comparison is made in FN layer thickness between this study and previous studies. In addition to conventional fuzzy layer thickness without W deposition from NAGDIS-II [33], PISCES-B [6], and Magnum-PSI [31], the fuzzy layer thickness with auxiliary W deposition in a magnetron sputtering device [17], height of initial growth phase of LFNs [16], and

Table 2: Summary of EDS analysis of W3, W5, W6, D1, and D2 at different positions.

Sample	position	W [at%]	Mo [at%]	Cu [at%]	Ca [at%]	Fe [at%]
W3	0 mm	73.3±0.8	25.4±0.5	0	1.3 ±0.5	0
W3	10 mm	93.3±0.7	5.8±0.7	0	1.0±0.3	0
W5	0 mm	7.1±0.3	17.3 ±0.4	50.3±0.5	10.8 ±0.5	14.6 ±0.8
W5	5 mm	84.4±0.7	11.0±0.6	3.5±2.6	1.1±0.6	0
W5	A (fuzz)	94.2±0.3	5.8±0.1	0	0	0
W5	B	97.0±0.3	2.3±0.1	0	0	0
W5	C (fuzz)	91.3±2.4	5.2±0.6	0	3.6±0.3	0
W5	D	97.1±2.1	2.9±0.4	0	0	0
W5	fuzz	75.1±11.9	14.3±0.6	3.6±2.7	0	7.0 ±11.2
W6	0 mm	95.8±1.5	4.2±2.0	0	0	0
W6	5 mm	96.9±2.6	3.1±2.0	0	0	0
D1	0 mm	95.5±1.6	4.5±2.0	0	0	0
D1	5 mm	95.7±1.5	4.3±2.4	0	0	0
D2	0 mm	95.2±1.8	4.7±5.5	0	0	0
D2	5 mm	96.2±0.8	3.6±3.4	0	0	0

thickness of LFNs in the latter growth phase [14] are shown as a function of the He fluence in Fig. 11. For W6 sample, considering the He fluence of 1.4×10^{26} m^{-2}, h_{FN} of 1.4 μm was consistent with the thickness of the conventional fuzz. On the other hand, h_{FN} of D1 and D2 was greater than the cases without deposition at the similar fluences. In the PISCES-B and Magnum-PSI devices, respectively, 6.5 μm thick and 7.5 μm thick fuzzy layers have been identified previously [18, 6]. However, the He fluence was about two orders of magnitudes greater than that of D1 and D2 (1×10^{28} m^{-2} in the PISCES-B and 3×10^{28} m^{-2} in the Magnum-PSI). Although the rate of acceleration was much less than the cases of LFNs in the NAGDIS-II, it is highly likely that an acceleration in the growth rate occurred by the additional deposition of W on D1 and D2 by a factor of 4-5.

4.2. TEM observation

Figure 12 shows a transmission electron microscope (TEM) micrograph of D1 sample from the bottom (right edge) to the top (left edge). The sample was cut by FIB to the thickness of less than 100 nm. Before cutting the sample, the sample was coated with a carbon ink to support the fuzz structures during and after the FIB milling. Thus, the white areas in Fig. 12 are occupied by the carbon based coating, and the black region corresponds to W. Near the bottom 500-nm-thick region, the width of FNs was slightly wider than that in the top region and density of structures seemed higher. When comparing with conventional fuzzy structures [33], it seems that the white area is more significant, suggesting that the density is less than that of the fuzz formed without W deposition.

Although D1 was covered with the ink and could not be used, we estimated the porosity of the fuzzy layer on D2 by measuring the mass of the fuzzy layer. First, we measured h_{FN} profiles using the CLSM; it was 6.8 μm at 0 mm, ≈5 μm at 4-7 mm, and decreased to 1.7 μm at 8 mm. In average, h_{FN} was estimated to be 4.8±0.5 μm using the area as a weight of average. The mass of the fuzzy layer was measured from the weight change after removing the layer from the sample. The density and porosity, p, were measured to be $4.5(-0.4,+0.6)\times10^2$ kg/m^3 and 97.7(+0.2,-0.3)%, respectively. The relative density of fuzzy layer, ρ, has been measured by Nishijima and his colleagues and was ≈8 and 6% when h_{FN} was 1.5 and 3 μm, respectively [10]. The relative density was 2.3(+0.3,-0.2)% on the fuzzy layer of D2 and was less than half of that at 3 μm fuzzy layer. However, the porosity of the fuzzy layer in Fig. 12 was much higher than that of mm-thick LFNs, which was 99.9% for rhenium case [34].

Figure 13 shows TEM micrographs with larger magnifications. Figure 13(a,b) shows the top and bottom (close to the substrate) regions, respectively. Many bubbles are identified inside the fibers, and sizes of the bubbles are distributed within the range of several nm to 20-30 nm in diameter. The shape of the bubbles are not spherical but faceted, elongated, and distorted. The width of the fibers is ∼20 nm in diameter on the top and roughly twice wider on the bottom region. Figure 13(c) shows a TEM microscope on the bottom part with a higher magnification. This region also has many bubbles, and like those in Fig. 13(a,b), the shapes are not spheres but faceted polyhedra.

When comparing them to fuzzy structures formed without deposition [33, 35], the difference in the fibers seemed insignificant. Though the thickness of the fuzzy layer and the porosity were different, the shapes of wires and bubbles inside were almost the same as those of fuzzy structures formed without deposition. On the other hand, clear differences can be seen from the LFNs formed with deposition in the NAGDIS-II device, where membrane structures and long wires have been found in the fuzzy layer which has a two orders of magnitude greater thickness [36]. The deposition rate is known to be an important parameter for the formation of LFNs, and the LFN growth occurred when the deposition rate was higher than $\sim2.5\times10^{18}$ m^{-2}s^{-1} [16]. In the present experiments, we could not measure the amounts of sputtering and deposition; it is of importance to investigate the relation between the deposition amount and the growth rate in various He flux ranges. It is necessary to consider

transport of W with collisional processes such as ionization and Coulomb collision to measure W flux. The mass change of the sample is another option to measure the deposition. However, because erosion of the sample also occurred at the same time, it is not straightforward to deduce the amount of deposition from the mass change.

Note that the sputtering yield of W by He ions increases by 59% when increasing the incident ion energy from 250 to 300 eV [37]. From spectroscopy, a line emission of W I at 400.9 nm was identified, and the line emission ratio of W I (400.9 nm) to He I (447.1 nm) increased from 0.19 (D1) to 0.52 (D2). The inconsistency between the theoretical values and spectroscopy was probably because of the effects of V_s and impurities. Although W influx should be increased considerably from D1 to D2, h_{FN} was almost the same between D1 and D2 and no W flux dependence was seen. The tendency was quite different from LFN cases [16], where the growth rate increased with W flux. In previous study, since the LFN grown from the edge was focused, the fuzzy layer grown on the base was not discussed. Previously, the LFNs growth was always initiated from edges of the sample close to the deposition source. However, the edge of the sample was not exposed to the plasma in this study, because the sample was clamped to the stage with a Mo holder, which covered the edge of the sample. Thus, it would be of interest to explore the irradiation experiments using the samples with grooves on the sample similar to the one used previously [38]. Except for the LFNs grown from the edge, the W flux dependence of the growth rate can be weak and easily saturate. It would be interesting to investigate the growth rate at much higher W flux in Magnum-PSI with a special setup to cool down the sputtering plate.

5. Conclusions

Non-uniform fuzz growth by helium plasma irradiations were identified on tungsten samples in the Magnum-PSI device. The fuzz growth often did not occur around the central region of the plasma column, while the fuzz growth occurred around the peripheral region (i.e. several mm away from the center). In the peripheral region, sometimes non-uniform fuzz growth and fuzzy island were identified. To understand the mechanism for the non-uniform fuzz formation, we performed potential profile measurement in some cases and impurity measurements using EDS and spectroscopy.

When the target potential was close to the floating potential, because the potential always has a well-shaped profile, the central region had a lower incident ion energy. This could counteract the fuzz growth near the center. However, the potential measurement using a reciprocating probe showed that the potential difference between the center and periphery was not significant, typically 5 eV, and this would not be the case when a negative biasing of the sample was significant. It was found that impurity line emission from the source (copper line) was always high when the fuzz was not grown at the center. Moreover, the EDS analysis revealed that impurity content around the center was higher than in the peripheral region in those cases. It was suggested that the impurity from the source inhibited the growth of fuzzy structures around the center by sputtering. Concerning the non-uniform fuzz growth around the periphery, the major reason was likely non-uniform temperature profiles. From the EDS analysis, the region of the fuzzy islands formed around the peripheral region of the sample had a higher impurity (mainly molybdenum) content (24.9±11.9%). With increasing the fraction of impurity, the melting point, T_m, decreases. It is known that fuzz growth window can be explained in the normalized surface temperature to the melting point, T_s/T_m. Thus, the local increase in impurity fraction would increase T_s/T_m locally, and consequently, satisfy fuzz growth condition in those regions. However, it is difficult to understand why locally high impurity regions were formed, and further experimental and theoretical works are necessary to totally elucidate the phenomena.

A tungsten plate was installed near the sample to simulate the deposition effects on helium plasma irradiation. In this experiment, because the plate was heated up quickly, we accumulated irradiation time by repeating short-time (20-25 s) irradiations. The thickness of fuzzy layer was ≈ 7 μm even though the He fluence was 1.3×10^{26} m^{-2}. Note that the thickness of fuzzy layer was 1.4 ± 0.3 μm at almost the same He fluence without deposition; the growth rate was accelerated by a factor of five with the deposition. It was shown that the enhanced fuzz growth can occur in high density ($\approx 4\times10^{19}$ m^{-3}) plasma conditions in addition to lower density cases previously reported ($\sim 10^{18}$ m^{-3} [14] and $\sim 10^{16}$ m^{-3} [17]. However, different from LFN cases where the growth rate was sensitive to the W flux [16], no significant difference was identified at different amount of sputtering (deposition) by changing the bias of the plate. The results suggested that the W influx dependence of fuzz growth on the base was different from that of LFN growth. Although the growth rate increased, we did not identify much greater (mm-thick) large-scale fiberform structures. It can be partially attributed to the fact that the large-scale structures were always grown from the edge of the sample, and there was no exposed edge to the plasma in the present experiments. For divertor tiles in ITER, for example, because there are many edges exposed to the plasma, the effects of deposition on the He plasma irradiation near the edge are of interest to investigate further.

Acknowledgement

This work was supported in part by a Grant-in-Aid for Scientific Research 19H01874, and Fund for the Promotion of Joint International Research 17KK0132 from the Japan Society for the Promotion of Science (JSPS).

References

[1] H. Iwakiri, K. Yasunaga, K. Morishita, N. Yoshida, Microstructure evolution in tungsten during low-energy helium ion irradiation, Journal of Nuclear Materials 283-287 (2000) 1134–1138.

[2] F. I. Allen, P. Hosemann, M. Balooch, Key mechanistic features of swelling and blistering of helium-ion-irradiated tungsten, Scripta Materialia 178 (2020) 256 – 260. doi:https://doi.org/10.1016/j.scriptamat.2019.11.039.
URL http://www.sciencedirect.com/science/article/pii/S1359646219306955

[3] S. Takamura, N. Ohno, D. Nishijima, S. Kajita, Formation of nanostructured tungsten with arborescent shape due to helium plasma irradiation, Plasma and Fusion Research 1 (2006) 051.

[4] S. Kajita, W. Sakaguchi, N. Ohno, N. Yoshida, T. Saeki, Formation process of tungsten nanostructure by the exposure to helium plasma under fusion relevant plasma conditions, Nucl. Fusion 49 (2009) 095005.

[5] M. Baldwin, R. Doerner, Helium induced nanoscopic morphology on tungsten under fusion relevant plasma conditions, Nucl. Fusion 48 (3) (2008) 035001 (5pp).
URL http://stacks.iop.org/0029-5515/48/035001

[6] T. Petty, M. Baldwin, M. Hasan, R. Doerner, J. Bradley, Tungsten 'fuzz' growth re-examined: the dependence on ion fluence in non-erosive and erosive helium plasma, Nuclear Fusion 55 (9) (2015) 093033.
URL http://stacks.iop.org/0029-5515/55/i=9/a=093033

[7] M. Baldwin, R. Doerner, Formation of helium induced nanostructure 'fuzz' on various tungsten grades, Journal of Nuclear Materials 404 (3) (2010) 165–173. doi:10.1016/j.jnucmat.2010.06.034.
URL http://www.sciencedirect.com/science/article/pii/S0022311510002849

[8] S. Takamura, T. Miyamoto, Recovery of tungsten surface with fiber-form nanostructure by the argon plasma irradiation at a high surface temperature, Plasma and Fusion Research 6 (2011) 1202005.

[9] S. Kajita, N. Yoshida, R. Yoshihara, N. Ohno, T. Yokochi, M. Tokitani, S. Takamura, TEM analysis of high temperature annealed W nanostructure surfaces, Journal of Nuclear Materials 421 (1-3) (2012) 22–27. doi:10.1016/j.jnucmat.2011.11.044.
URL http://www.sciencedirect.com/science/article/pii/S0022311511009998

[10] D. Nishijima, M. Baldwin, R. Doerner, J. Yu, Sputtering properties of tungsten 'fuzzy' surfaces, Journal of Nuclear Materials 415 (2011) S96–S99.

[11] R. Doerner, M. Baldwin, P. Stangeby, An equilibrium model for tungsten fuzz in an eroding plasma environment, Nucl. Fusion 51 (4) (2011) 043001.
URL http://stacks.iop.org/0029-5515/51/i=4/a=043001

[12] Y. Noiri, S. Kajita, N. Ohno, Nanostructure growth by helium plasma irradiation to tungsten in sputtering regime, Journal of Nuclear Materials 463 (2015) 285–288. doi:http://dx.doi.org/10.1016/j.jnucmat.2015.01.036.
URL http://www.sciencedirect.com/science/article/pii/S0022311515000483

[13] G. D. Temmerman, R. Doerner, R. Pitts, A growth/annealing equilibrium model for helium-induced nanostructure with application to ITER, Nuclear Materials and Energy 19 (2019) 255 – 261. doi:https://doi.org/10.1016/j.nme.2019.01.034.
URL http://www.sciencedirect.com/science/article/pii/S2352179118302862

[14] S. Kajita, S. Kawaguchi, N. Ohno, N. Yoshida, Enhanced growth of large-scale nanostructures with metallic ion precipitation in helium plasmas, Sci. Rep. 8 (2018) 56.

[15] D. Hwangbo, S. Kajita, N. Ohno, P. McCarthy, J. W. Bradley, H. Tanaka, Growth of nano-tendril bundles on tungsten with impurity-rich He plasmas, Nuclear Fusion 58 (9) (2018) 096022. doi:10.1088/1741-4326/aacd1f.
URL https://doi.org/10.1088%2F1741-4326%2Faacd1f

[16] S. Kajita, S. Kawaguchi, N. Yoshida, N. Ohno, H. Tanaka, Morphologies of co-depositing W layer formed during He plasma irradiation, Nucl. Fusion 58 (2018) 106002.

[17] P. McCarthy, D. Hwangbo, M. Bilton, S. Kajita, J. W. Bradley, Enhanced fuzzy tungsten growth in the presence of tungsten deposition, Nuclear Fusion 60 (2) (2020) 026012. doi:10.1088/1741-4326/ab6060.
URL https://doi.org/10.1088%2F1741-4326%2Fab6060

[18] M. Balden, S. Elgeti, T. W. Morgan, S. Brezinsek, G. D. Temmerman, Scanning electron microscopy analyses of an ITER plasma-facing unit mockup exposed to extreme ion fluences in magnum-PSI, Physica Scripta T171 (2020) 014026. doi:10.1088/1402-4896/ab4479.
URL https://doi.org/10.1088%2F1402-4896%2Fab4479

[19] J. Rapp, W. Koppers, H. van Eck, G. van Rooij, W. Goedheer, B. de Groot, R. Al, M. Graswinckel, M. van den Berg, O. Kruyt, P. Smeets, H. van der Meiden, W. Vijvers, J. Scholten, M. van de Pol, S. Brons, W. Melissen, T. van der Grift, R. Koch, B. Schweer, U. Samm, V. Philipps, R. Engeln, D. Schram, N. L. Cardozo, A. Kleyn, Construction of the plasma-wall experiment magnum-PSI, Fusion Engineering and Design 85 (7) (2010) 1455 – 1459. doi:https://doi.org/10.1016/j.fusengdes.2010.04.009.
URL http://www.sciencedirect.com/science/article/pii/S092037961000150X

[20] H. J. van der Meiden, A. R. Lof, M. A. van den Berg, S. Brons, A. J. H. Donné, H. J. N. van Eck, P. M. J. Koelman, W. R. Koppers, O. G. Kruijt, N. N. Naumenko, T. Oyevaar, P. R. Prins, J. Rapp, J. Scholten, D. C. Schram, P. H. M. Smeets, G. van der Star, S. N. Tugarinov, P. A. Z. van Emmichoven, Advanced Thomson scattering system for high-flux linear plasma generator, Review of Scientific Instruments 83 (12) (2012) 123505. doi:10.1063/1.4768527.
URL http://link.aip.org/link/?RSI/83/123505/1

[21] S. Kajita, G. Akkermans, K. Fujii, H. van der Meiden, M. C. M. van de Sanden, Emission spectroscopy of He lines in high-density plasmas in magnum-psi, AIP Advances 10 (2) (2020) 025225. arXiv:https://doi.org/10.1063/1.5143481, doi:10.1063/1.5143481.
URL https://doi.org/10.1063/1.5143481

[22] R. A. Felice, Temperature determining device and process, US Patent 6,379,038 (Apr. 30 2002).

[23] K. D. Hammond, Helium, hydrogen, and fuzz in plasma-facing materials, Materials Research Express 4 (10) (2017) 104002.

[24] P. Stangeby, The Plasma Boundary of Manegic Fusion Devices, IoP Publishing, Bristol and Philadelphia, 2000.

[25] N. Ohno, M. Seki, H. Ohshima, H. Tanaka, S. Kajita, Y. Hayashi, H. Natsume, H. Takano, I. Saeki, M. Yoshikawa, H. van der Meiden, Investigation of recombination front region in detached plasmas in a linear divertor plasma simulator, Nuclear Materials and Energy 19 (2019) 458 – 462. doi:https://doi.org/10.1016/j.nme.2019.03.010.
URL http://www.sciencedirect.com/science/article/pii/S2352179118302540

[26] J. Holman, Heat Transfer, McGraw-Hill, 2009.

[27] S. Kajita, T. Yokochi, N. Ohno, T. Kumano, Near infrared radiation from heated nanostructured tungsten, Jpn. J. Appl. Phys. 51 (2012) 01AJ03.

[28] N. Ohno, Y. Hirahata, M. Yamagiwa, S. Kajita, M. Takagi, N. Yoshida, R. Yoshihara, T. Tokunaga, M. Tokitani, Influence of crystal orientation on damages of tungsten exposed to helium plasma, Journal of Nuclear Materials 438, Supplement (2013) S879–S882. doi:http://dx.doi.org/10.1016/j.jnucmat.2013.01.190.
URL http://www.sciencedirect.com/science/article/pii/S0022311513001980

[29] J. Scholten, P. Zeijlmans van Emmichoven, H. van Eck, P. Smeets, G. De Temmerman, S. Brons, M. van den Berg, H. van der Meiden, M. van de Pol, M. Graswinckel, P. Groen, A. Poelman, J. Genuit, Operational status of the magnum-PSI linear plasma device, Fusion Engineering and Design 88 (9) (2013) 1785 – 1788. doi:https://doi.org/10.1016/j.fusengdes.2013.05.063.
URL http://www.sciencedirect.com/science/article/pii/S0920379613005036

[30] S. Kajita, T. Nojima, Y. Tomita, N. Ohno, H. Tanaka, N. Yoshida, M. Yajima, T. Akiyama, M. Tokitani, T. Yagi, Fuzzy nanostructure growth on precious metals by He plasma irradiation, Surface and Coatings Technology 340 (2018) 86–92. doi:https://doi.org/10.1016/j.surfcoat.2018.02.026.
URL http://www.sciencedirect.com/science/article/pii/S025789721830135X

[31] T. W. Morgan, M. Balden, T. Schwarz-Selinger, Y. Li, T. H. Loewenhoff, M. Wirtz, S. Brezinsek, G. D. Temmerman, ITER monoblock performance under lifetime loading conditions in magnum-PSI, Physica Scripta T171 (2020) 014065. doi:10.1088/1402-4896/ab66df.
URL https://doi.org/10.1088%2F1402-4896%2Fab66df

[32] S. V. Nagender-Naidu, A. M. Sriramamurthy, P. R. Rao, The Mo-W (molybdenum-tungsten) system, Bulletin of Alloy Phase Diagrams 5 (1984) 177–180.

[33] S. Kajita, N. Yoshida, R. Yoshihara, N. Ohno, M. Yamagiwa, TEM observation of the growth process of helium nanobubbles on tungsten: Nanostructure formation mechanism, Journal of Nuclear Materials 418 (1-3) (2011) 152–158. doi:10.1016/j.jnucmat.2011.06.026.
URL http://www.sciencedirect.com/science/article/pii/S0022311511005885

[34] S. Kajita, T. Nojima, T. Okuyama, Y. Yamamoto, N. Yoshida, N. Ohno, Helium-plasma–induced straight nanofiber growth on hcp metals, Acta Materialia 181 (2019) 342–351.

[35] G. De Temmerman, K. Bystrov, J. J. Zielinski, M. Balden, G. Matern, C. Arnas, L. Marot, Nanostructuring of molybdenum and tungsten surfaces by low-energy helium ions, Journal of Vacuum Science & Technology A 30 (4) (2012) 041306. doi:http://dx.doi.org/10.1116/1.4731196.
URL http://scitation.aip.org/content/avs/journal/jvsta/30/4/10.1116/1.4731196

[36] S. Kajita, N. Yoshida, S. Kawaguchi, H. Tanaka, N. Ohno, D. Nagata, M. Tokitani, Growth of membrane nanostructures on W co-deposition layer, Nuclear Materials and Energy 18 (2019) 339 – 344. doi:https://doi.org/10.1016/j.nme.2019.02.004.
URL http://www.sciencedirect.com/science/article/pii/S2352179118301455

[37] W. Eckstein, Calculated sputtering, reflection and range values, IPP (2002) 9/132.

[38] M. Yajima, N. Ohno, S. Kajita, G. D. Temmerman, K. Bystrov, S. Bardin, T. Morgan, S. Masuzaki, Investigation of arcing on fiber-formed nanostructured tungsten by pulsed plasma during steady state plasma irradiation, Fusion Engineering and Design 112 (2016) 156–161. doi:https://doi.org/10.1016/j.fusengdes.2016.07.026.
URL http://www.sciencedirect.com/science/article/pii/S0920379616305348

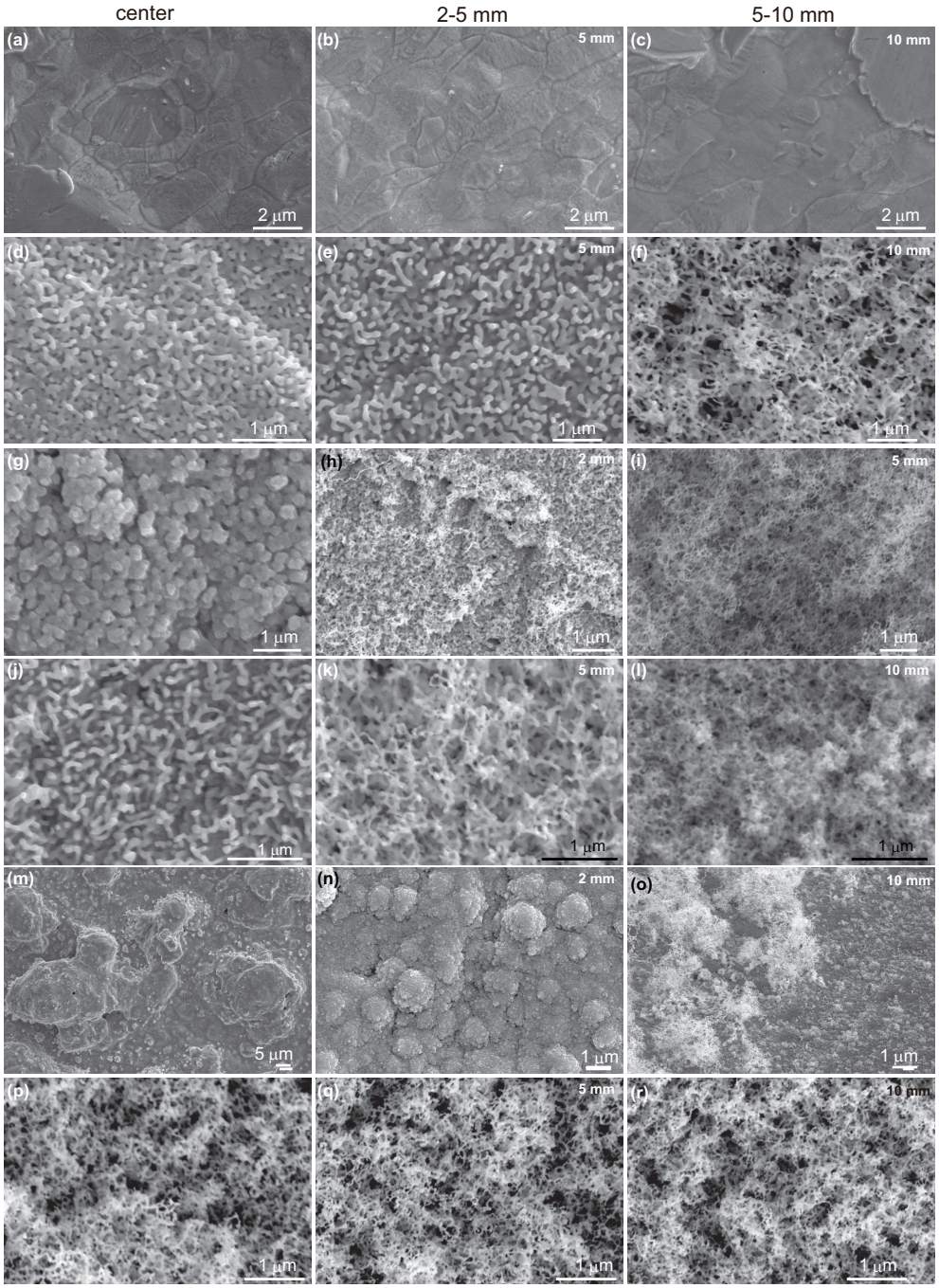

Figure 4: SEM micrographs of (a-c) W1 ($V_W = -13$ V), (d-f) W2 ($V_W = -22$ V), (g-i) W3 ($V_W = -34$ V), (j-l) W4 ($V_W = -45$ V), (m-o) W5 ($V_W = -55$ V), and (p-r) W6 ($V_W = -62$ V) at three different locations, i.e. at the center (leftmost), 2-5 mm (center), and 5-10 mm (rightmost).

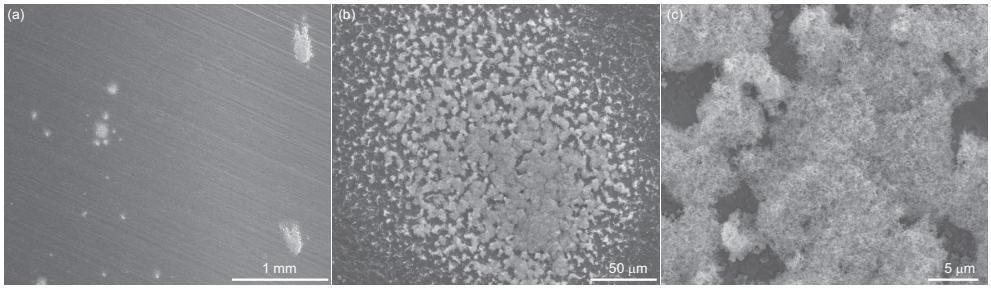

Figure 5: SEM micrographs of the peripheral region of W5 at different magnifications. In (b), one of the white areas in (a) is shown in a larger magnification. In the white areas, FNs are grown locally, as shown in (c).

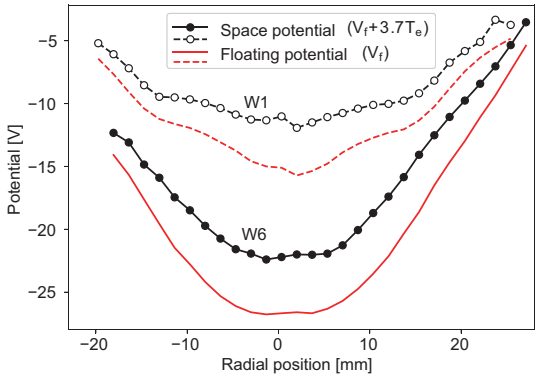

Figure 6: Two typical profiles of the floating and space potential for the irradiation conditions of W1 and W6 measured using the reciprocating probe.

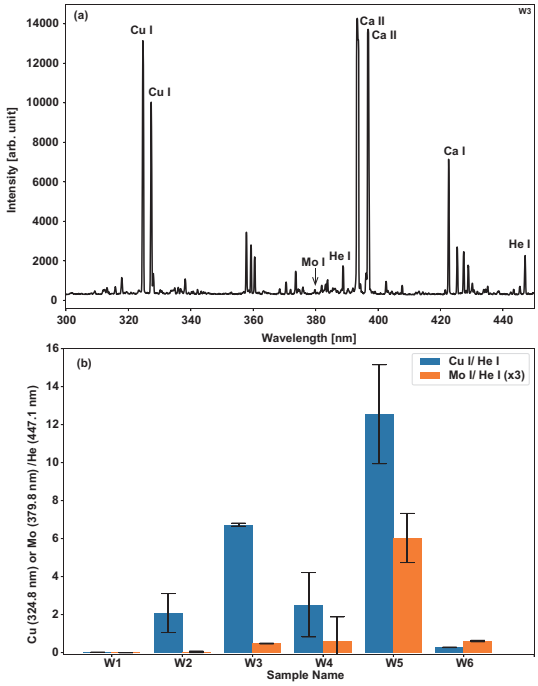

Figure 7: (a) Spectrum in the wavelength range of 300-450 nm when W3 was exposed and (b) the line intensity ratios of Cu I at 324.8 nm and Mo I at 379.8 nm to He I at 447.1 nm for W1-W6 samples.

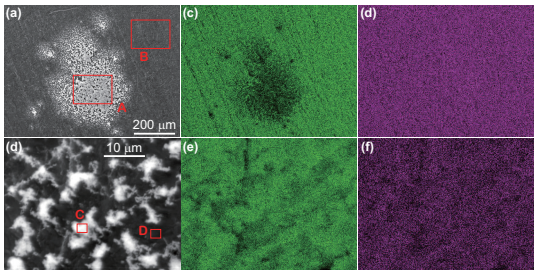

Figure 8: EDS mappings of sample W5 around fuzz region at $r \sim 10$ mm at two areas ((a,b,c) and (d,e,f)) with different magnifications. (a,d) SEM images, (c,e) W signal profiles, and (d,f) Mo signal profiles. White region in (a,d) corresponds fuzz areas.

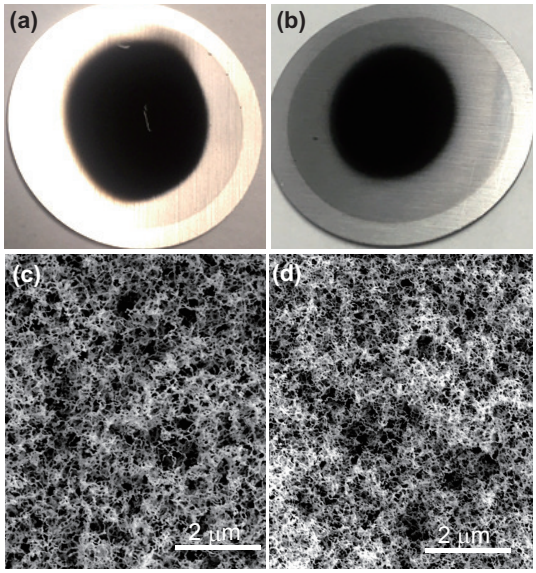

Figure 9: (a,b) Pictures of D1 and D2 samples, respectively, and (c,d) SEM micrographs at the irradiation center of D1 and D2 samples, respectively. Different from W1-6 samples, a negatively biased (-250 V for D1 and -300 V for D2) W sputtering plate was installed near the sample for sputtering source.

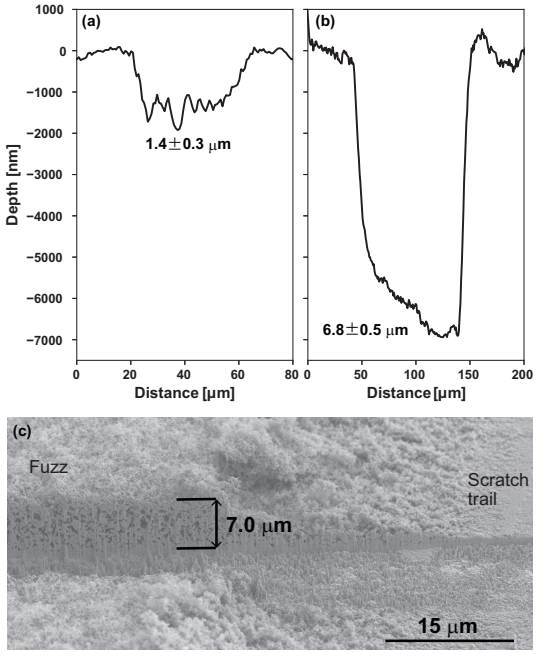

Figure 10: (a,b) The depth profiles measured by CLSM around scratches on W6 and D2 samples, respectively, and (c) an SEM micrograph of FIB cut D1 sample around the scratch. From this method, the fuzzy layer thickness was measured to be 1.4 ± 0.3 and 6.8 ± 0.5 μm for W6 and D2, respectively. From the cross section of D1 sample shown in (c), the validity of the method was confirmed.

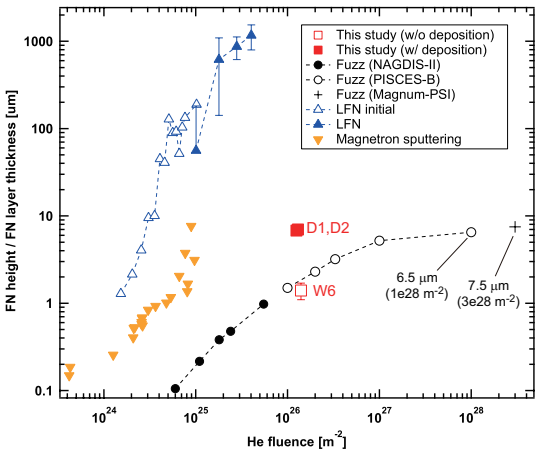

Figure 11: A comparison in FN layer thickness as a function of He fluence between this study (red squares) and previous studies: conventional fuzzy layer thickness without W deposition from NAGDIS-II [33], PISCES-B [6], and Magnum-PSI [31], the fuzzy layer thickness with auxiliary W deposition in a magnetron sputtering device [17], height of initial growth phase of LFNs [16], and thickness of LFNs in the latter growth phase [14].

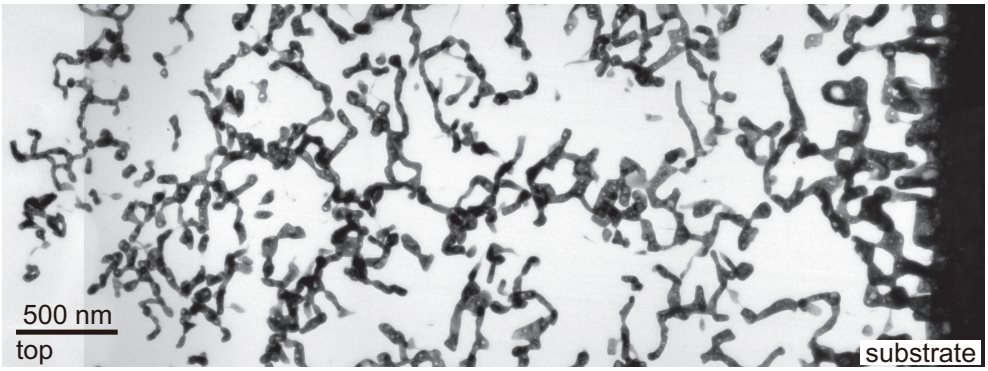

Figure 12: A TEM micrograph of D1 sample from the bottom (right edge) to the top (left edge).

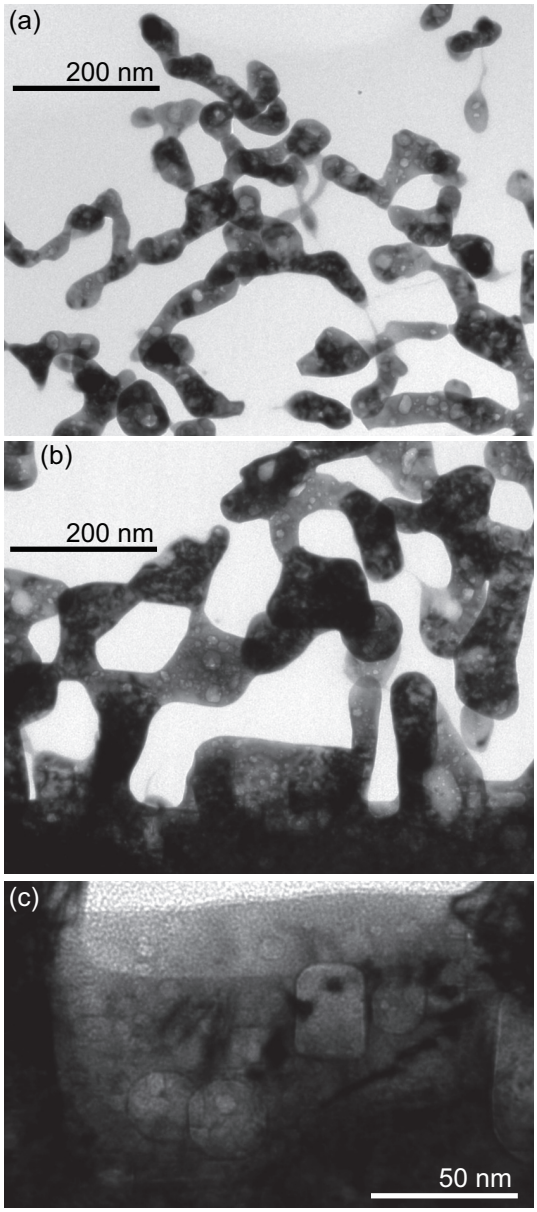

Figure 13: TEM micrographs with larger magnifications (a) at the top and (b,c) bottom (close to the substrate).